

Halo assembly bias and the tidal anisotropy of the local halo environment

Aseem Paranjape^{1*}, Oliver Hahn^{2†} & Ravi K. Sheth^{3,4‡}

¹ *Inter-University Centre for Astronomy & Astrophysics, Ganeshkhind, Post Bag 4, Pune 411007, India*

² *Laboratoire Lagrange, Université Côte d’Azur, Observatoire de la Côte d’Azur, CNRS, Blvd de l’Observatoire, CS 34229, 06304 Nice cedex 4, France*

³ *Center for Particle Cosmology, University of Pennsylvania, 209 S. 33rd St., Philadelphia, PA 19104, USA*

⁴ *The Abdus Salam International Center for Theoretical Physics, Strada Costiera, 11, Trieste 34151, Italy*

draft

ABSTRACT

We study the role of the local tidal environment in determining the assembly bias of dark matter haloes. Previous results suggest that the anisotropy of a halo’s environment (i.e. whether it lies in a filament or in a more isotropic region) can play a significant role in determining the eventual mass and age of the halo. We statistically isolate this effect using correlations between the large-scale and small-scale environments of simulated haloes at $z = 0$ with masses between $10^{11.6} \lesssim (m/h^{-1}M_{\odot}) \lesssim 10^{14.9}$. We probe the large-scale environment using a novel halo-by-halo estimator of linear bias. For the small-scale environment, we identify a variable α_R that captures the *tidal anisotropy* in a region of radius $R = 4R_{200b}$ around the halo and correlates strongly with halo bias at fixed mass. Segregating haloes by α_R reveals two distinct populations. Haloes in highly isotropic local environments ($\alpha_R \lesssim 0.2$) behave as expected from the simplest, spherically averaged analytical models of structure formation, showing a *negative* correlation between their concentration and large-scale bias at *all* masses. In contrast, haloes in anisotropic, filament-like environments ($\alpha_R \gtrsim 0.5$) tend to show a *positive* correlation between bias and concentration at any mass. Our multi-scale analysis cleanly demonstrates how the overall assembly bias trend across halo mass emerges as an average over these different halo populations, and provides valuable insights towards building analytical models that correctly incorporate assembly bias. We also discuss potential implications for the nature and detectability of galaxy assembly bias.

Key words: cosmology: theory, dark matter, large-scale structure of the Universe – methods: numerical

1 INTRODUCTION

The assembly history of dark matter haloes is known to correlate with the large scale environment, even for haloes of fixed current mass (Sheth & Tormen 2004; Gao et al. 2005). This effect, known as *halo assembly bias*, has been well studied in the literature using N -body simulations, and extends to several halo properties including age, accretion rate, concentration, spin, shape, velocity dispersion and anisotropy, etc. (see, e.g. Wechsler et al. 2006; Jing et al. 2007; Desjacques 2008; Hahn et al. 2009; Fakhouri & Ma 2010; Faltenbacher & White 2010; Borzyszkowski et al. 2017; Paranjape & Padmanabhan 2017; Lazeyras et al. 2017). To the

extent that galaxy formation and evolution is regulated by the accretion of dark matter onto the host halo of a galaxy, assembly bias can in principle have interesting observational consequences (Zentner et al. 2014; Hearin et al. 2016). While there have been several recent observational attempts at detecting assembly bias effects in galaxy and cluster populations (Lin et al. 2016; Miyatake et al. 2016; Montero-Dorta et al. 2017), systematic effects in cleanly segregating galaxy populations have been challenging to overcome (Tinker et al. 2016; Zu et al. 2016).

The assembly bias trend seen in numerical studies is that, at large halo mass, highly concentrated or old haloes cluster weakly as compared to less concentrated or younger haloes of the same mass. At low mass on the other hand, the trend inverts, with old haloes clustering *more* strongly than younger ones. The trend for massive haloes is, in fact, qualitatively predicted by simple models of structure formation

* E-mail: aseem@iucaa.in

† E-mail: oliver.hahn@oca.eu

‡ E-mail: shethrk@physics.upenn.edu

based on peaks theory (Dalal et al. 2008), ellipsoidal dynamics (Desjacques 2008) or the excursion set formalism (Musso & Sheth 2012; Castorina & Sheth 2013). In these models, assembly bias arises from a strong correlation between the density structure of a Lagrangian ‘proto-halo’ patch that is destined to become a virialised halo and its larger scale density environment. These strong correlations naturally produce haloes with large inner density (or high concentration) which form early and live in more underdense environments as compared to haloes of the same mass but with lower inner density, that form late and live in denser environments. The peaks and/or excursion set models, however, predict that this qualitative trend should be seen at *any* fixed mass, and therefore contradict the inversion of the trend around $m \sim m_*$ as seen in simulations, where m_* is the scale where the mass fraction in haloes has a maximum. The inversion is therefore likely to be associated with some key physical criterion that the models are currently missing.

One plausible mechanism for explaining the inversion was proposed by Hahn et al. (2009). These authors argued that low mass haloes in filaments suffer tidal truncation of their mass accretion due to redirected mass flows along their filament, with the degree of truncation depending on the magnitude of anisotropic velocity shear in the vicinity of the halo. This has been further established by Borzyszkowski et al. (2017) using zoom simulations of individual low mass haloes in a variety of tidal environments (see also Behroozi et al. 2014). In the present work, we further explore the role of the tidal environment in establishing the inversion of the low mass assembly bias trend using a multi-scale statistical study of N -body simulations. Our aim is to identify the key statistical variable (there may be more than one) that controls the sign of the correlation between halo properties such as age or concentration and their large scale bias. Our expectation is that such a study will provide clear guidance for how tidal effects might be included in analytical models of halo abundances and clustering that correctly incorporate assembly bias at all mass scales.

The paper is organised as follows. In section 2 we describe our N -body simulations and the construction of an object-by-object linear bias estimator \hat{b}_1 that becomes a valuable tool for studying multi-scale correlations. In section 3 we establish a statistical link between the large scale halo environment (as measured by \hat{b}_1) and the *anisotropy* of the halo’s local tidal environment. In particular, we identify a scalar combination α_R of the eigenvalues of the tidal tensor smoothed on scale $R = 4R_{200b}$ ¹ at the halo location and show that α_R correlates more strongly with \hat{b}_1 than does the overdensity δ_R on the same scale. Then, in section 4, we study halo assembly bias as a function of tidal anisotropy, by measuring the correlation between \hat{b}_1 and halo concentration (a proxy for halo age) as a function of α_R . This allows us to link halo internal properties with both the small scale tidal environment and the large scale density around the halo. We discuss the implications of this multi-scale study for understanding the origin of assembly bias in section 5,

and conclude in section 6. The Appendices give technical details of some of the results used in the main text.

Throughout, we use a spatially flat Lambda cold dark matter (Λ CDM) cosmology with total matter density parameter $\Omega_m = 0.276$, baryonic matter density $\Omega_b = 0.045$, Hubble constant $H_0 = 100h \text{ km s}^{-1} \text{ Mpc}^{-1}$ with $h = 0.7$, primordial scalar spectral index $n_s = 0.961$ and r.m.s. linear fluctuations in spheres of radius $8h^{-1} \text{ Mpc}$, $\sigma_8 = 0.811$, with a transfer function generated by the code CAMB (Lewis et al. 2000).²

2 NUMERICAL TECHNIQUES

Below, we describe the N -body simulations used in this work, followed by a description of a novel object-by-object estimator of halo clustering that we will use in our analysis.

2.1 N -body simulations

We have performed N -body simulations of CDM using the tree-PM code GADGET-2 (Springel 2005)³ with $N_p = 1024^3$ particles in a cubic, periodic box of comoving length $L_{\text{box}} = 300h^{-1} \text{ Mpc}$ and a 2048^3 PM grid, with force resolution $\epsilon = 9.8h^{-1} \text{ kpc}$ comoving. For our chosen cosmology, this gives a particle mass of $m_p = 1.93 \times 10^9 h^{-1} M_\odot$. As we will see, this configuration allows us to straddle the characteristic mass scale m_* of the halo mass function at $z = 0$ with sufficient dynamic range to probe both the regimes of assembly bias mentioned earlier. Initial conditions were generated at a starting redshift $z_{\text{in}} = 49$ using the code MUSIC (Hahn & Abel 2011)⁴ with 2nd order Lagrangian perturbation theory (2LPT). Haloes were identified using the code ROCKSTAR (Behroozi et al. 2013)⁵ which performs a Friends-of-Friends (FoF) algorithm in 6-dimensional phase space. The simulations and analysis were performed on the Perseus cluster at IUCAA.⁶

To ensure that our results are not contaminated by substructure and numerical artefacts, we discard all sub-haloes, as well as objects whose ‘virial’ energy ratio $\eta = 2T/|U|$ satisfies $\eta \geq 2$ (corresponding to unbound objects). Below, we will heavily rely on measurements of the tidal environment in the vicinity of the haloes. These measurements are performed after Gaussian smoothing on a cubic grid with $N_g = 512^3$ cells. We therefore impose a restriction on the minimum halo mass we study, so as to minimise the contamination to our final results from the resolution imposed by this grid. We describe our procedure in Appendix A; this leads to a minimum halo mass $m_{200b} \geq m_{\text{min}} \simeq 3.1 \times 10^{12} h^{-1} M_\odot$, corresponding to haloes resolved with $N_p^{(\text{halo})} \geq 1600$ particles each. These cuts leave us with approximately 38,700 objects on average at $z = 0$ in a single realisation of the simulation. Additionally, throughout the analysis we impose an upper limit of $m_{200b} \leq m_{\text{max}} = 7.7 \times 10^{14} h^{-1} M_\odot$, corresponding to the mass scale above which we expect fewer than 10 haloes for our box size and cosmology at $z = 0$.

¹ R_{200b} is defined as the radius where the enclosed density is 200 times the background density. The mass enclosed inside R_{200b} is denoted m_{200b} .

² <http://camb.info>

³ <http://www.mpa-garching.mpg.de/gadget/>

⁴ <https://www-n.oica.eu/ohahn/MUSIC/>

⁵ <http://code.google.com/p/rockstar/>

⁶ <http://hpc.iucaa.in>

To improve our statistics, we have generated 10 realisations of our simulation by changing the seed for the initial conditions. For some of our statistical results, we will also additionally use the output of a single realisation of a simulation with the same cosmology, number of particles and PM grid, but having $L_{\text{box}} = 150h^{-1}\text{Mpc}$ and a force resolution $\epsilon = 4.9h^{-1}\text{kpc}$, which will extend our mass range down to $m_{200b} \gtrsim 3.85 \times 10^{11}h^{-1}M_{\odot}$. We will refer to this as the high resolution box, and to the 10 larger volume realisations as the default box. Throughout, we will focus on results at $z = 0$.

2.2 Halo-by-halo estimator of bias

Traditional estimators of halo bias involve ratios of (cross) power spectra of haloes and dark matter. Exploiting some basic properties of discrete Fourier transforms, we construct an object-by-object estimator of large-scale linear halo bias, whose average properties reproduce known trends derived from traditional estimators. This new halo-by-halo bias then becomes a useful probe of the correlations between large-scale and small-scale halo environment, and between these two and other halo properties such as assembly history, halo (sub-)structure, etc. We give the details of our construction below.

The traditional cross-correlation based estimator of halo bias in Fourier space is the ratio of the halo-matter cross power spectrum $P_{\text{hm}}(k)$ and the matter auto power spectrum $P_{\text{mm}}(k)$:

$$b_{\text{hm}}(k) \equiv P_{\text{hm}}(k)/P_{\text{mm}}(k) \quad (1)$$

At large scales ($k \rightarrow 0$), this recovers the ‘peak-background split’ value of Eulerian linear bias (Paranjape & Sheth 2012; Schmidt et al. 2013). It is instructive to recapitulate the procedure for deriving the halo-matter cross power spectrum in a simulation box. In the following, we will consider a collection of haloes indexed by the integer variable h whose values are restricted according to some condition \mathcal{C} . E.g., \mathcal{C} could refer to selecting haloes in a chosen mass bin. Starting with the positions $\{\mathbf{x}_h\}$ of all haloes in a (cubic, periodic) simulation of volume V_{box} and a grid with N_{g} cubic cells, we define the number overdensity of \mathcal{C} -haloes $\delta_{\text{halo}}(\mathbf{x}|\mathcal{C})$ at the grid cell with position \mathbf{x} as

$$\begin{aligned} \delta_{\text{halo}}(\mathbf{x}|\mathcal{C}) &\equiv n_{\text{halo}}(\mathbf{x}|\mathcal{C})/\bar{n}_{\text{halo}}(\mathcal{C}) - 1 \\ &= \sum_{h \in \mathcal{C}} N_{\text{g}} \vartheta(\mathbf{x}, \mathbf{x}_h) / \sum_{h \in \mathcal{C}} -1 \end{aligned} \quad (2)$$

where $\vartheta(\mathbf{x}, \mathbf{x}_h)$ is a selection function that gives the contribution of halo h with position \mathbf{x}_h to the cell at \mathbf{x} and satisfies $\sum_{\{\mathbf{x}\}} \vartheta(\mathbf{x}, \mathbf{x}_h) = 1$ when summed over the grid, so that the \mathcal{C} -halo number density is the sum over \mathcal{C} -haloes⁷ $n_{\text{halo}}(\mathbf{x}|\mathcal{C}) = \sum_{h \in \mathcal{C}} \vartheta(\mathbf{x}, \mathbf{x}_h)$, with mean number density

$$\bar{n}_{\text{halo}}(\mathcal{C}) = \sum_{\{\mathbf{x}\}} n_{\text{halo}}(\mathbf{x}|\mathcal{C}) / \sum_{\{\mathbf{x}\}} = \sum_{h \in \mathcal{C}} 1/N_{\text{g}}, \quad (3)$$

since $\sum_{\{\mathbf{x}\}} = N_{\text{g}}$.

⁷ This is the discretized version of the continuum result $n_{\text{halo}}(\mathbf{x}|\mathcal{C}) = \sum_{h \in \mathcal{C}} \delta_{\text{D}}(\mathbf{x} - \mathbf{x}_h)$.

The discrete Fourier transform of $\delta_{\text{halo}}(\mathbf{x}|\mathcal{C})$ can then be manipulated as follows:

$$\begin{aligned} \delta_{\text{halo}}(\mathbf{k}|\mathcal{C}) &\equiv \frac{1}{N_{\text{g}}} \sum_{\{\mathbf{x}\}} e^{i\mathbf{k} \cdot \mathbf{x}} \delta_{\text{halo}}(\mathbf{x}|\mathcal{C}) \\ &= \left[\sum_{h \in \mathcal{C}} \sum_{\{\mathbf{x}\}} e^{i\mathbf{k} \cdot \mathbf{x}} \vartheta(\mathbf{x}, \mathbf{x}_h) / \sum_{h \in \mathcal{C}} \right] - \sum_{\{\mathbf{x}\}} e^{i\mathbf{k} \cdot \mathbf{x}} / N_{\text{g}} \\ &= \sum_{h \in \mathcal{C}} e^{i\mathbf{k} \cdot \mathbf{x}(h)} / \sum_{h \in \mathcal{C}} - \delta_{\mathbf{k}, \mathbf{0}}^{\text{Kronecker}}, \end{aligned} \quad (4)$$

where we used the shorthand notation $e^{i\mathbf{k} \cdot \mathbf{x}(h)}$ to denote the appropriate weighted sum of phase factors over all cells receiving a contribution from halo h .⁸ Ignoring the Kronecker delta which enforces $\delta_{\text{halo}}(\mathbf{k} = \mathbf{0}|\mathcal{C}) = 0$, we are left with

$$\delta_{\text{halo}}(\mathbf{k}|\mathcal{C}) = \sum_{h \in \mathcal{C}} e^{i\mathbf{k} \cdot \mathbf{x}(h)} / \sum_{h \in \mathcal{C}}, \quad \text{for } \mathbf{k} \neq \mathbf{0}. \quad (5)$$

A similar calculation holds for the matter density fluctuation field $\delta(\mathbf{k})$, but we will not need its explicit form below.

The required power spectra then follow from taking averages in spherical shells of \mathbf{k} ; denoting these by $\langle \rangle_k$, we have

$$\begin{aligned} P_{\text{hm}}(k|\mathcal{C}) &= V_{\text{box}} \langle \delta_{\text{halo}}(\mathbf{k}|\mathcal{C}) \delta^*(\mathbf{k}) \rangle_k \\ &= V_{\text{box}} \sum_{h \in \mathcal{C}} \left\langle e^{i\mathbf{k} \cdot \mathbf{x}(h)} \delta^*(\mathbf{k}) \right\rangle_k / \sum_{h \in \mathcal{C}}, \\ P_{\text{mm}}(k) &= V_{\text{box}} \langle \delta(\mathbf{k}) \delta^*(\mathbf{k}) \rangle_k, \end{aligned} \quad (6)$$

where the asterisk denotes a complex conjugate. The expression (1) for k -dependent linear bias of \mathcal{C} -haloes then reduces to

$$\begin{aligned} b_{\text{hm}}(k|\mathcal{C}) &= \sum_{h \in \mathcal{C}} \left(\frac{V_{\text{box}}}{P_{\text{mm}}(k)} \left\langle e^{i\mathbf{k} \cdot \mathbf{x}(h)} \delta^*(\mathbf{k}) \right\rangle_k \right) / \sum_{h \in \mathcal{C}} \\ &\equiv \sum_{h \in \mathcal{C}} b_{1,h}(k) / \sum_{h \in \mathcal{C}} \end{aligned} \quad (7)$$

where the second line defines an object-by-object, scale dependent quantity $b_{1,h}(k)$ whose average over the haloes under consideration corresponds to the usual scale-dependent cross-correlation linear bias. Notice that the selection criterion \mathcal{C} only appears in defining the average by restricting the summation range.

We can reduce $b_{1,h}(k)$ to a single number for each halo by averaging over low- k modes⁹ for which the bias is expected to be nearly constant:

$$\begin{aligned} \hat{b}_{1,h} &\equiv \sum_{\text{low } k} N_k b_{1,h}(k) / \sum_{\text{low } k} N_k \\ &= \sum_{\text{low } k} N_k \left(V_{\text{box}} \left\langle e^{i\mathbf{k} \cdot \mathbf{x}(h)} \delta^*(\mathbf{k}) \right\rangle_k / P_{\text{mm}}(k) \right) / \sum_{\text{low } k} N_k, \end{aligned} \quad (8)$$

⁸ Our notation corresponds to the exact result for the nearest grid point (NGP) scheme, with $\mathbf{x}(h)$ in this case being the location of the single cell that contains halo h . For the cloud-in-cell (CIC) scheme, which we use in practice, $e^{i\mathbf{k} \cdot \mathbf{x}(h)}$ stands for a weighted sum over eight cells.

⁹ For the analysis in this paper, we use $0.025 \lesssim k/(h\text{Mpc}^{-1}) \lesssim 0.09$ for our default box, and $0.05 \lesssim k/(h\text{Mpc}^{-1}) \lesssim 0.09$ for the high resolution box.

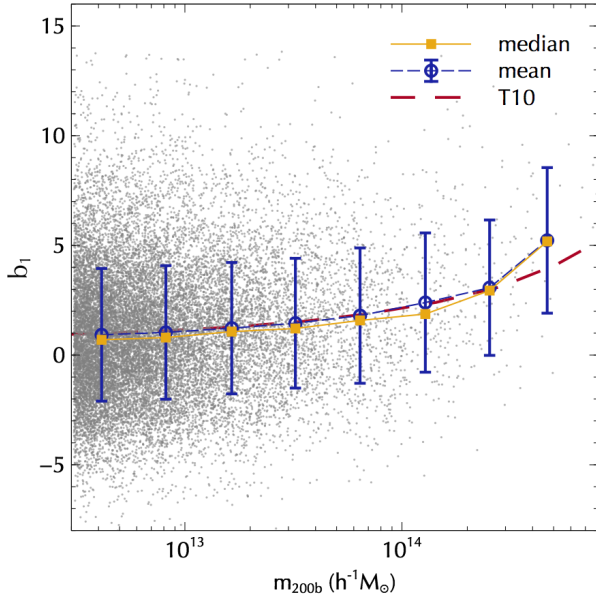


Figure 1. Halo-by-halo bias. Gray points show measurements of \hat{b}_1 (equation 8) for individual haloes in an N -body simulation as a function of halo mass $m = m_{200b}$, randomly downsampled to 20,000 objects. Points show the median (filled yellow squares) and mean (open blue circles) of \hat{b}_1 in bins of halo mass. Error bars indicate the scatter (standard deviation) in each mass bin. Smooth dashed curve shows the fitting function for linear bias appropriate for m_{200b} -haloes taken from [Tinker et al. \(2010\)](#).

where we have weighted by the number of modes $N_k \propto k^3$ for logarithmically spaced bins. We will refer to this quantity $\hat{b}_{1,h}$, defined for every halo h , as halo-by-halo bias. For ease of notation, we will drop the subscript h whenever no confusion can arise.

This definition of halo-by-halo bias has several useful properties. Firstly, our derivation above shows that \hat{b}_1 averages to the usual peak-background split bias for any choice of halo selection criterion \mathcal{C} (e.g., binning by mass). Being defined for each halo, however, makes \hat{b}_1 a convenient additional property that can be included in a halo catalog and studied in conjunction with any other halo property of interest, *without* any need for binning in principle. The gray points in Figure 1 show measurements of halo-by-halo bias and halo mass for individual haloes in one simulation box. The filled yellow and open blue points respectively show the median and mean of \hat{b}_1 in bins of halo mass, while the dashed red curve shows the fitting function from [Tinker et al. \(2010\)](#). We see that, as expected, there is good agreement between the measurements and the fit at all but the highest masses which suffer from volume effects and possibly also some mild scale dependence due to our choice of k range.

The most striking aspect of the Figure, however, is the large scatter in \hat{b}_1 . The standard deviation of \hat{b}_1 , shown by the error bars on the measurements of the mean, is about $\sigma_{b_1} \simeq 3$ at essentially all masses. (Note that the error on the mean is much smaller, due to the large number of points in each bin.) At low masses, this means that the small value of mean or median halo bias is, in fact, a rather poor indicator of the large scale environment of these objects. Below, we will explore the relation between this scatter in \hat{b}_1 and the

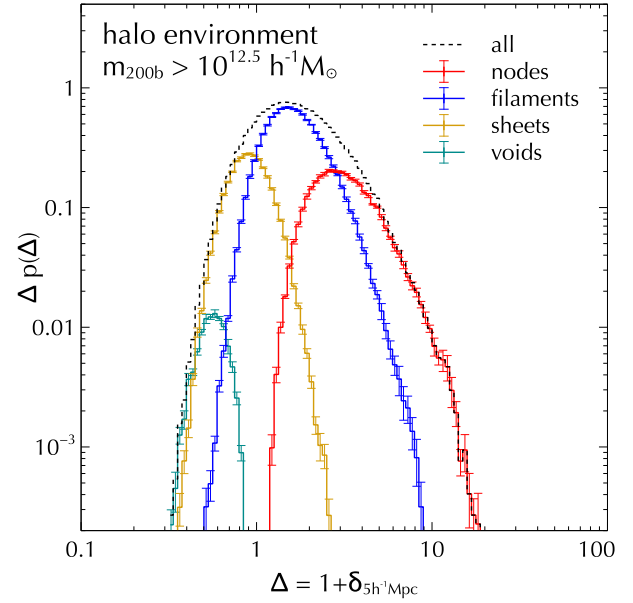


Figure 2. Dark matter density in halo environments. Histograms show the distribution of overdensity $1 + \delta_R$ centered on haloes selected as described in the text and smoothed with a Gaussian window of radius $R = 5h^{-1}\text{Mpc}$, averaged over 10 realisations of the default box. The error bars indicate the standard error on the mean over the 10 realisations. Dashed histogram shows the total distribution, while the various colours indicate different halo environments (from right to left in order of peak location: nodes, filaments, sheets and voids).

properties of the local environment of the haloes populating the tails of the distribution.

3 LARGE SCALE HALO BIAS AND SMALL SCALE ENVIRONMENT

Much of the analysis below will involve studying the connection between halo clustering at large scales and the tidal environment of the haloes at small or intermediate scales. Our main goal in this section is to identify a convenient variable that quantifies the tidal anisotropy of the immediate halo environment, whose correlation with the *large scale* environment can then be a probe of assembly bias. As a warm-up, let us first explore the relation between the halo-by-halo bias variable \hat{b}_1 defined above and the simplest variable that characterises halo environment, namely, the dark matter density contrast δ_R smoothed on some fixed large scale R .

3.1 Correlation between \hat{b}_1 and δ_R

In Figure 2, we show the distribution of $1 + \delta_R$ centered on haloes and smoothed with a Gaussian window of radius $R = 5h^{-1}\text{Mpc}$. This was done by first computing δ on a $N_g = 512^3$ grid using CIC interpolation and smoothing in Fourier space (i.e., multiplying $\delta(\mathbf{k})$ with $e^{-k^2 R^2/2}$), and then transforming back to real space and interpolating the smoothed field to the locations of the haloes to get δ_R . We used all haloes in a realisation that passed the cuts discussed in section 2 and averaged over 10 realisations of the default

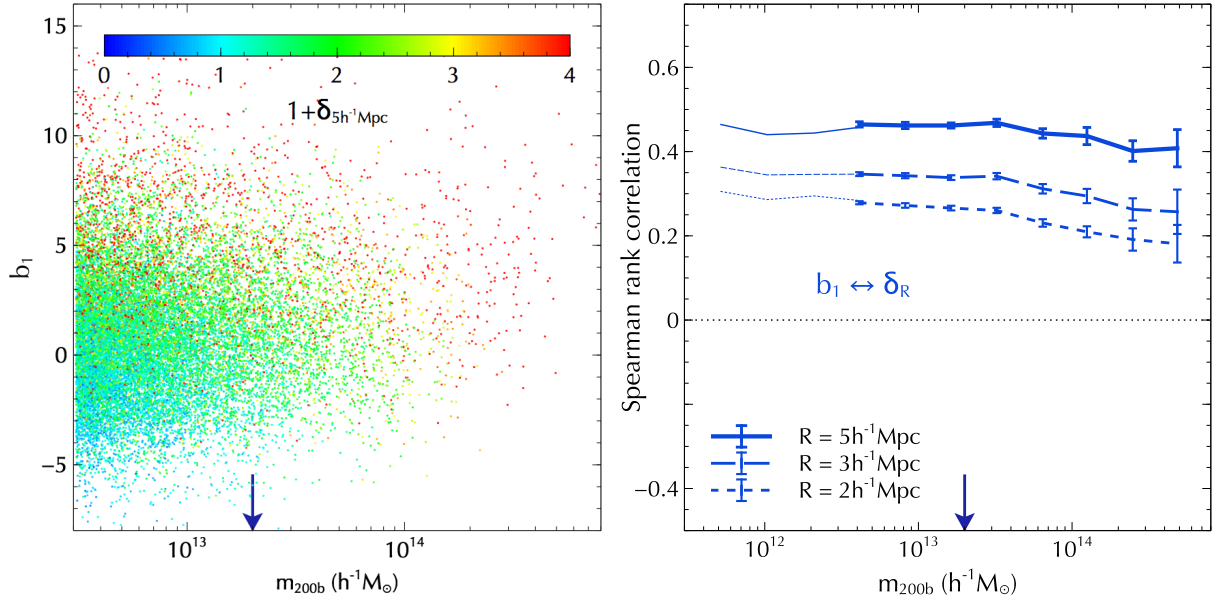


Figure 3. (*Left panel:*) Halo-by-halo bias against halo mass, with the points coloured according to $1 + \delta_{5h^{-1}\text{Mpc}}$, i.e., the halo-centric overdensity Gaussian-smoothed on scale $5h^{-1}\text{Mpc}$. (*Right panel:*) Spearman rank correlation coefficient between \hat{b}_1 and δ_R for $R = 2, 3, 5h^{-1}\text{Mpc}$ as indicated (thick lines), averaged over 10 realisations of the default box, with the error bars showing the standard error on the mean. The thin lines extending to low masses show the results of the single high resolution box. The arrow in each panel marks the characteristic mass m_* obtained from the peak of the halo mass distribution function.

box. We have split the distribution in Figure 2 as arising from four categories – nodes, filaments, voids and sheets – determined by the number of positive eigenvalues of the tidal tensor T_{ij} (Hahn et al. 2007) as described in Appendix B.

The *left panel* of Figure 3 shows the scatter plot of \hat{b}_1 and mass, coloured by $1 + \delta_{5h^{-1}\text{Mpc}}$. There is an obvious correlation visible, with a largely vertical trend in which \hat{b}_1 increases monotonically with $\delta_{5h^{-1}\text{Mpc}}$. This trend is consistent with previous results in the literature, which have shown that large scale bias is more strongly correlated with halo-centric overdensity than it is with halo mass (see, e.g., Abbas & Sheth 2007). The *right panel* of the Figure explores this further, showing the Spearman rank correlation coefficient between \hat{b}_1 and δ_R as a function of halo mass, for $R = 2, 3, 5h^{-1}\text{Mpc}$. We see that the strength of the correlation is only a weak function of mass for each smoothing scale, but monotonically increases with R . This increase with R is not surprising, since our estimator for \hat{b}_1 itself is ultimately measuring a large scale halo-centric overdensity, so that \hat{b}_1 and δ_R are measuring essentially the same quantity for large R . In Appendix C1, we present analytical arguments that explain the size of the scatter in \hat{b}_1 at fixed mass and also qualitatively reproduce the trends seen in Figure 3.

The variable δ_R at fixed smoothing scale R might seem to be a natural choice for determining environmental properties. We see in Figure 2, however, that $\delta_{5h^{-1}\text{Mpc}}$ is not a particularly strong discriminator of environment into nodes, filaments, etc., and we have checked that similar results are true at smaller smoothing scales as well. There is also not much to be gained by smoothing at fixed larger scales, either, since we are ultimately interested in the tidal environment on scales close to the halo size, which would physically correspond to the tidal forces being experienced by individual haloes. We therefore conclude that we should look for vari-

ables defined close to the halo size that discriminate between different environments better than δ_R , and also correlate more strongly with \hat{b}_1 than does δ_R .

3.2 Tidal anisotropy α_R

The rotational invariants of the tidal tensor T_{ij} beyond its trace δ_R are a natural starting point in looking for discriminatory variables. One such variable q_R^2 , sometimes referred to in the literature as tidal shear, is particularly promising. This is defined as (Heavens & Peacock 1988; Catelan & Theuns 1996)

$$q_R^2 \equiv I_1^2 - 3I_2 = \frac{1}{2} [(\lambda_3 - \lambda_1)^2 + (\lambda_3 - \lambda_2)^2 + (\lambda_2 - \lambda_1)^2], \quad (9)$$

where $\lambda_1 \leq \lambda_2 \leq \lambda_3$ are the eigenvalues of T_{ij} and $I_1 = \lambda_1 + \lambda_2 + \lambda_3$ and $I_2 = \lambda_1\lambda_2 + \lambda_2\lambda_3 + \lambda_3\lambda_1$ are its first two rotational invariants. A closely related variable $s^2 = 2q^2/3$ has been used in the recent literature in the context of measuring ‘non-local’ bias (Chan et al. 2012; Baldauf et al. 2012; Saito et al. 2014).

For a *Gaussian* random field, the shear q_R^2 has the remarkable property that its distribution is *independent* of the trace δ_R (and can be shown to be Chi-squared with 5 degrees of freedom, see Sheth & Tormen 2002). In general, q_R^2 reflects the anisotropy of the tidal environment at any scale R , vanishing for a perfectly isotropic environment. In terms of the more commonly used anisotropy measures ‘ellipticity’ $e_R \equiv (\lambda_3 - \lambda_1)/2\delta_R$ and ‘prolateness’ $p_R \equiv (\lambda_3 - 2\lambda_2 + \lambda_1)/2\delta_R$ (e.g., Bardeen et al. 1986; Bond & Myers 1996), we have¹⁰ $q_R^2 = \delta_R^2 (3e_R^2 + p_R^2)$. So we expect

¹⁰ Note that Bardeen et al. (1986) used the ellipticity and pro-

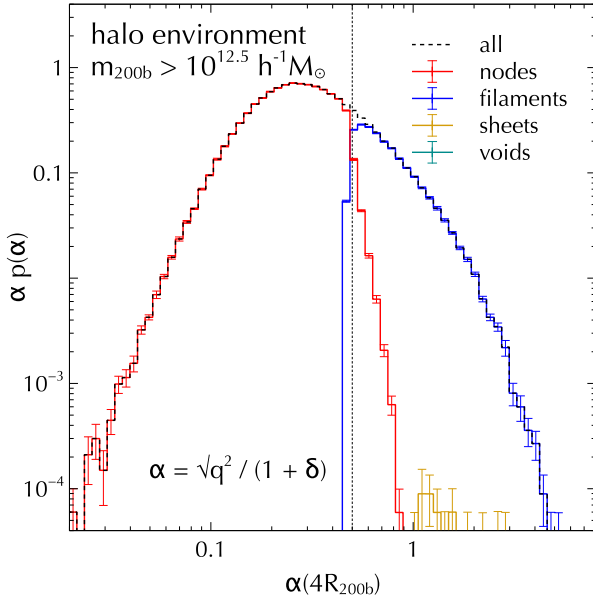


Figure 4. Tidal anisotropy in halo environments. Histograms show the distribution of α_R (equation 10) centered on haloes selected as described in the text and smoothed with a Gaussian window of radius $R = R_{G,\text{eff}}^{(4R_{200b})}$ (equations A9 and A11), averaged over 10 realisations of the default box. The error bars indicate the standard error on the mean over the 10 realisations. Dashed histogram shows the total distribution, while the various colours indicate different halo environments: essentially no sheet or void environments are measured, and there is a sharp distinction between filaments ($\alpha_R \gtrsim 0.5$) and nodes ($\alpha_R \lesssim 0.5$, compare Figure 2).

that q_R^2 defined close to the halo scale should retain substantial information regarding the tidal anisotropy of the halo environment.

For the *non-linear* dark matter field, unfortunately, q_R^2 is quite strongly correlated with δ_R . To see why this is to be expected, consider that the density contrast in 2LPT can be written in terms of the Gaussian-field δ and q^2 as $\delta_{2\text{LPT}} = \delta + (17/21)\delta^2 + (4/21)q^2$. Approximating the nonlinear shear by its value for the Gaussian field then already shows that one might expect the correlation coefficient between q_R^2 and δ_R to be $\simeq 0.12\sigma \times (1 + \mathcal{O}(\sigma^2))$ at scales where 2LPT is valid, where $\sigma^2 = \langle \delta^2 \rangle = \langle q^2 \rangle$, with a stronger correlation at smaller scales. This means that any correlation q_R might have with \hat{b}_1 could easily be contaminated by the correlation between \hat{b}_1 and δ_R , and not necessarily be a measure of anisotropy alone.

After some experimentation, we have found that the following variable has the properties we require for quantifying tidal anisotropy at the halo scale, beyond what is measured by δ_R :

$$\alpha_R \equiv (1 + \delta_R)^{-1} \sqrt{q_R^2}. \quad (10)$$

lateness defined with the Hessian of the overdensity field, $\partial_i \partial_j \delta_R$, while Bond & Myers (1996) distinguished between these and analogous quantities defined using the tidal tensor T_{ij} . The variables we refer to above correspond to the latter; e_v and p_v in the notation of Bond & Myers (1996).

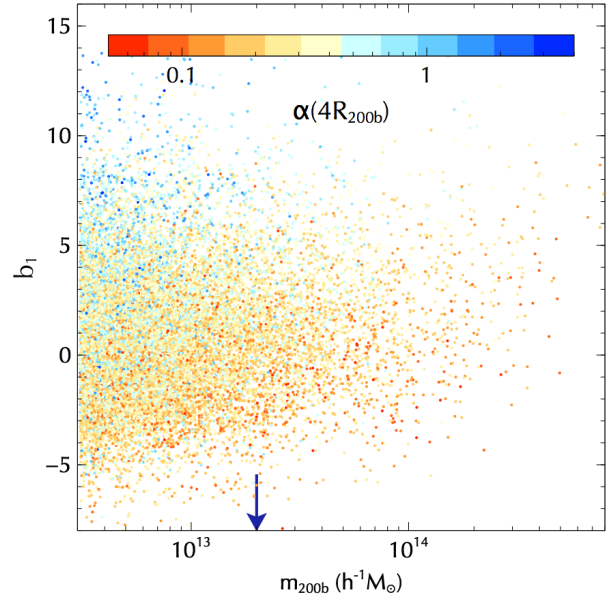


Figure 5. Halo-by-halo bias against halo mass, with the points coloured according to α_R (equation 10) smoothed with a Gaussian window of radius $R = R_{G,\text{eff}}^{(4R_{200b})}$ (equations A9 and A11). The arrow marks the characteristic mass m_* obtained from the peak of the halo mass distribution function.

We demonstrate this next with a series of measurements. Before we do so, however, it is worth mentioning that we have also explored analogous variables constructed using the Hessian of the density $\partial_i \partial_j \delta_R$. Indeed, several studies in the past have attempted to define the large scale environment through the density and its derivatives (see, e.g. Aragón-Calvo et al. 2007; Sousbie 2011). We find, however, that these tend to be poorer discriminators of the local web environment than the variables based on the tidal tensor. We have not explored variables based on the velocity shear $(\partial_i v_j + \partial_j v_i)/2$ (Hahn et al. 2009; Hoffman et al. 2012) which would differ from the tidal tensor due to nonlinear evolution. In principle, one might make more objective statements by comparing the utility of variables defined using the tidal tensor, density Hessian or velocity shear using information theoretic criteria such as those proposed by Leclercq et al. (2016); however, this is beyond the scope of the present work.

3.3 Correlation between \hat{b}_1 and tidal anisotropy

Figure 4 is formatted similarly to Figure 2 and shows the distribution of α_R defined at $R = R_{G,\text{eff}}^{(4R_{200b})}$, the Gaussian equivalent of $4R_{200b}$ (see equations A9 and A11), for haloes with $N_p^{(\text{halo})} \geq 1600$ averaged over 10 realisations of the default box. At these scales, essentially *no* halo is classified as being in a sheet or void, which is easy to understand if we consider that, as $R \rightarrow R_{200b}$, the immediate environment of a halo must be dominated by infall of matter onto the halo. We clearly see that α_R sharply distinguishes between filament and node environments, with $\alpha_R \gtrsim 0.5$ ($\alpha_R \lesssim 0.5$) corresponding to filaments (nodes).

Figure 5 is similar to the left panel of Figure 3, with the points now coloured by α_R defined at $4R_{200b}$. We see that haloes classified as being in filamentary environments

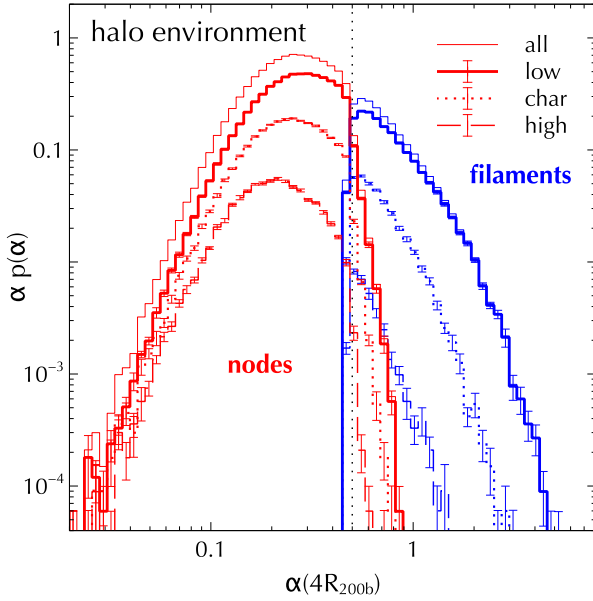


Figure 6. Similar to Figure 4, showing histograms only for nodes and filaments averaged over 10 realisations of the default box, with the histograms now split into three bins of halo mass – **low**: $m_{\min} \leq m < m_*/3$ (thick solid); **char**: $m_*/3 \leq m < 2m_*$ (dotted); **high**: $2m_* \leq m < m_{\max}$ (long dashed), where m_{\min} and m_{\max} were defined in section 2. Thin solid histograms show the respective sums over the three bins for nodes and filaments.

at this scale ($\alpha_R \gtrsim 0.5$, blueish colours) tend to have masses $m < m_*$. There is a clear indication that the highest values of \hat{b}_1 at $m < m_*$ in the left panel arise predominantly from haloes in filaments. We will return to this when discussing assembly bias below.

Figure 6 is similar to Figure 4, with the histograms now split into three bins of halo mass, with masses substantially below, close to and substantially above the characteristic mass m_* , respectively. We clearly see that filamentary haloes are dominated by the lowest mass bin. To see that this is not simply a consequence of the lowest mass bin being the most populous, note that the combined distribution of node+filament haloes in each mass bin forms an envelope whose median decreases from low to high masses. On the other hand, the transition between node and filament remains sharp and fixed at $\alpha_R \simeq 0.5$. Together, this makes the *fraction* of haloes in any mass bin that are classified as being in filaments *decrease* with increasing halo mass. The results of our high resolution box (not shown) are qualitatively consistent with these, with the distribution of α_R at the lowest masses extending to somewhat larger values.

Figure 7 shows a visualisation of the haloes in a subvolume of our high resolution box, with haloes shown as circles whose radii scale with R_{200b} and whose colour scales with the tidal anisotropy α_R defined at $R = R_{G,\text{eff}}^{(4R_{200b})}$. The panels focus on massive (*top*) and low mass haloes (*bottom*). Keeping in mind the histograms in Figure 6, we see that haloes with green to blue colours ($\alpha_R \gtrsim 0.5$) are classified as being in filament environments at the halo scale, while yellow to red colours correspond to node environments. It is then clear from the bottom panel that low mass haloes classified as being in filaments do, in fact, visually trace out

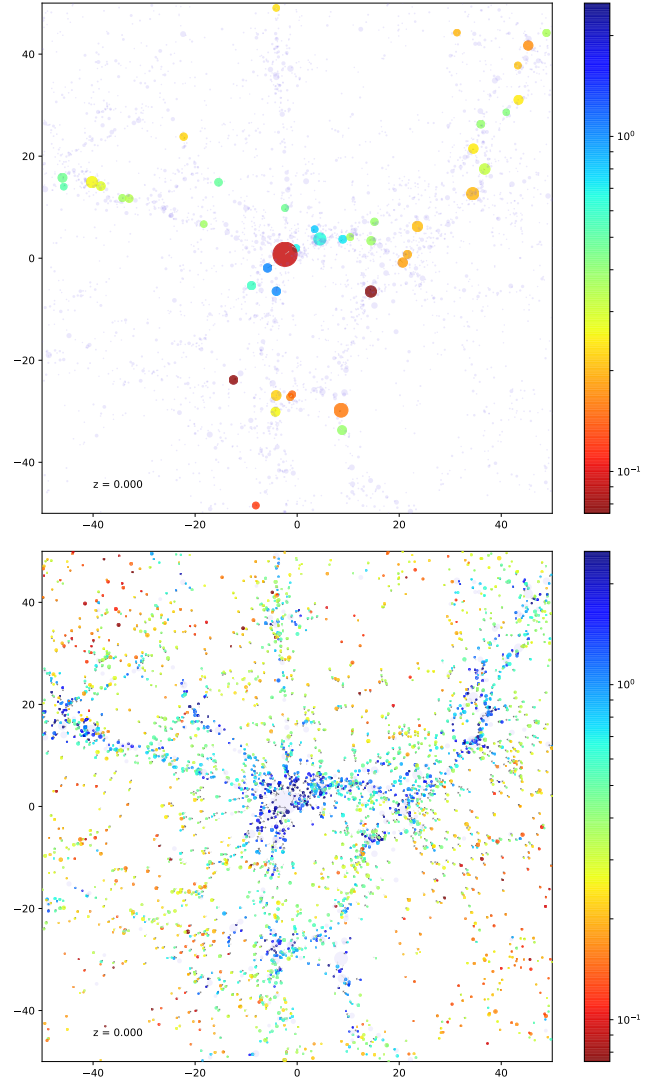


Figure 7. Visualisation of haloes in a $100h^{-1}\text{Mpc} \times 100h^{-1}\text{Mpc} \times 30h^{-1}\text{Mpc}$ volume in the high resolution box, centered on the halo with the largest value of α_R with $R = R_{G,\text{eff}}^{(4R_{200b})}$ and projected along the $30h^{-1}\text{Mpc}$ direction. Circles indicate the locations of haloes, with the radius of each circle being $1.5R_{200b}$ (to scale). Opaque coloured circles in the *top panel* correspond to massive haloes with $m > 2m_*$, with the colour scaling logarithmically according to the value of α_R for each halo as indicated by the colour bar. Similarly, the *bottom panel* focuses on low mass haloes with $m_{\min} < m < m_*/3$. Arrows on the opaque circles indicate the halo bulk velocity, scaled up for clarity to the straight-line distance the halo would travel in $800h^{-1}\text{Myr}$. The light (dark) coloured arrows indicate velocities pointing out of (into) the plane of the paper. Transparent blue circles in each panel indicate all haloes with $m > m_{\min}$ that are not in the respective bin. For this plot, we use $m_{\min} = 3.85 \times 10^{11}h^{-1}M_{\odot}$ (see section 2). Haloes classified as being in anisotropic local environments ($\alpha_R \gtrsim 0.5$, blueish colours), particularly the low-mass haloes in the *bottom panel*, clearly trace out large-scale filaments. Haloes with $\alpha_R \lesssim 0.2$ (reddish colours), on the other hand, are associated with either dense clusters (massive haloes in the *top panel*) or underdense void-like regions (low-mass haloes in the *bottom panel*). Low-mass haloes in the most anisotropic environments are predominantly associated with nearby massive haloes that generate strong tidal effects in their vicinity.

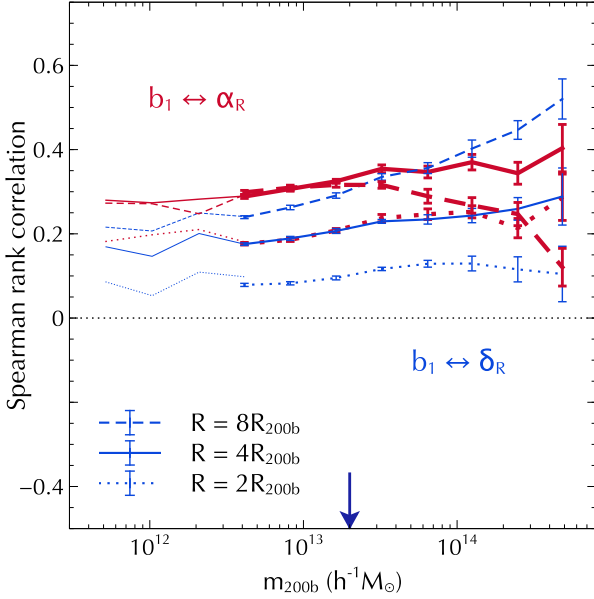


Figure 8. Spearman rank correlation coefficient between \hat{b}_1 and α_R (red, thick) for $R = R_{G,\text{eff}}^{(2R_{200b})}$ (dotted), $R_{G,\text{eff}}^{(4R_{200b})}$ (solid) and $R_{G,\text{eff}}^{(8R_{200b})}$ (dashed) averaged over 10 realisations of the default box, with error bars indicating the error on the mean of the 10 realisations. For comparison, the correlation between \hat{b}_1 and δ_R for the same smoothing scales is displayed as the thinner blue curves. The thinnest lines extending to low masses show the corresponding results of the single high resolution box. The arrow marks the characteristic mass m_* obtained from the peak of the halo mass distribution function.

filamentary structures and also predominantly occur in the vicinity of massive objects (which are themselves classified as being in nodes at their correspondingly larger smoothing scale). And low mass haloes far from any massive haloes are predominantly classified as being in nodes. We will see later that the distinction more relevant for assembly bias in fact occurs at smaller values of tidal anisotropy, $\alpha_R \simeq 0.2$.

Figure 8 shows the Spearman rank correlation between \hat{b}_1 and α_R (red, thick) as a function of halo mass, smoothed at the Gaussian equivalent of $2R_{200b}$ (dotted), $4R_{200b}$ (solid) and $8R_{200b}$ (dashed). For comparison, we also display the corresponding correlation between \hat{b}_1 and δ_R (blue, thin) at each smoothing scale (c.f. Figure 3). For $2R_{200b}$ and $4R_{200b}$, we see that there is a statistically significant *positive* correlation between \hat{b}_1 and α_R , which is *stronger* than the corresponding correlation between \hat{b}_1 and δ_R .¹¹ Also, the $\hat{b}_1 \leftrightarrow \alpha_R$ correlation is stronger at $4R_{200b}$ than at $2R_{200b}$. At $8R_{200b}$, on the other hand, we see that (a) the $\hat{b}_1 \leftrightarrow \alpha_R$ correlation is generally *weaker* than at $4R_{200b}$ and (b) the correlation between δ_R and \hat{b}_1 is generally stronger than that between α_R and \hat{b}_1 . In Appendix C2, we argue that the size of the sphere around the halo that is currently decoupling from the Hubble flow and turning around is likely to be close to $4\text{--}6R_{200b}$, which might plausibly explain why the tidal anisotropy on this scale shows the strongest correlation with large scale en-

¹¹ Notice that, had we set R to be the equivalent of R_{200b} , we would expect essentially *no* correlation between δ_R and \hat{b}_1 , since the former would be simply $\simeq 199$ for *every* halo.

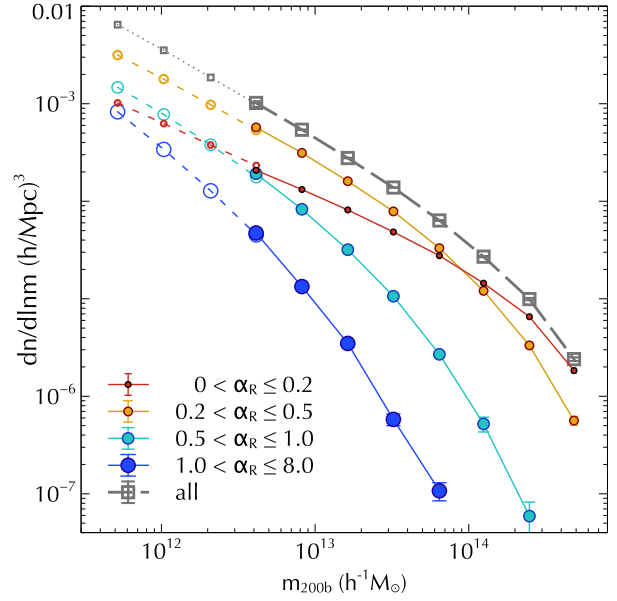


Figure 9. Halo mass function in bins of α_R for $R = R_{G,\text{eff}}^{(4R_{200b})}$ averaged over 10 realisations of our default box (filled circles, with error bars indicating the error on the mean in 10 realisations). For comparison, the empty gray squares show the mass function of all haloes. The empty symbols joined by thin lines extending to low masses show the results of the single high resolution box.

vironment. Combined with the behaviour of the histograms of α_R in different web environments, the results of Figure 8 validate our claim that this variable, when defined close to the halo scale (we will use the Gaussian equivalent of $4R_{200b}$ hereon), is a better indicator than δ_R of the relation between \hat{b}_1 and the degree of tidal anisotropy around haloes.

Figure 9 shows the halo mass function of all haloes (gray squares) and of haloes split into four bins of α_R for $R = R_{G,\text{eff}}^{(4R_{200b})}$ with edges given by $\alpha_R = \{0.0, 0.2, 0.5, 1.0, 8.0\}$ (filled circles, size increases with α_R). The bins with the two higher α_R values therefore approximately correspond to filamentary environments according to the standard classification, c.f. Figure 6). We see that the mass function steadily moves to smaller characteristic masses as α_R increases beyond $\gtrsim 0.2$. The mass function in highly isotropic environments with $0 < \alpha_R < 0.2$, however, dominates only at high masses and falls below that in anisotropic environments at smaller masses. This can be understood using Figure 10, which shows the fraction of haloes residing in $5h^{-1}\text{Mpc}$ node, filament, sheet and void environments, where the haloes were selected to be those in the most isotropic *local* environments, satisfying $\alpha_R < 0.125$ for $R = R_{G,\text{eff}}^{(4R_{200b})}$. As expected, at high masses these haloes continue to be classified as being in large scale node environments. At the lowest masses, on the other hand, most of these locally isotropic haloes live in large scale sheet and void environments. The low α_R mass function is therefore a combination of the mass function in dense clusters and sheets/voids.

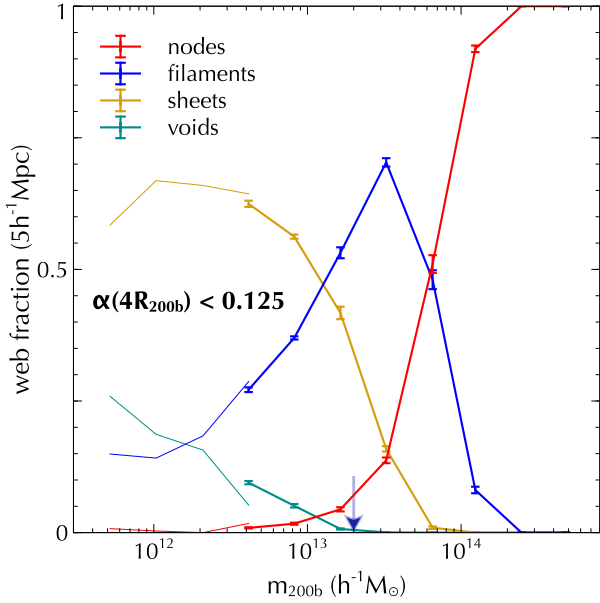


Figure 10. Fraction of haloes residing in $5h^{-1}\text{Mpc}$ node, filament, sheet and void environments (distributions favouring higher to lower masses, respectively). Haloes were selected to be those in the most isotropic *local* environments, satisfying $\alpha_R < 0.125$ for $R = R_{\text{G,eff}}^{(4R_{200b})}$. Results are averaged over 10 realisations of our default box, with error bars indicating the error on the mean in 10 realisations. The thin lines extending to low masses show the results of the single high resolution box. The arrow marks the characteristic mass m_* obtained from the peak of the halo mass distribution function.

4 ASSEMBLY BIAS

As discussed in the Introduction, it is interesting to theoretically explore the nature of assembly bias and the role played by the tidal environment of haloes in determining the sign and strength of the correlation between internal halo properties and their large scale clustering (Hahn et al. 2009). We do this below using our halo-by-halo bias estimator \hat{b}_1 .

4.1 Traditional estimates

Our definition of halo-by-halo bias \hat{b}_1 allows us to almost trivially reproduce known results on the large scale clustering of haloes split by any halo property. All that is needed is to calculate the mean value of \hat{b}_1 in appropriately chosen (multi-variate) bins. Focusing for example on halo concentration – defined in our case as $c_{200b} = R_{200b}/r_s$ where r_s is the scale radius obtained from fitting an NFW profile to the halo mass distribution – Figure 11 shows the mean bias as a function of halo mass, for all haloes in the mass bin (circles) and for haloes in the upper and lower quartiles of concentration (respectively, upward and downward pointing triangles). We clearly see the well known trend that, at high masses, low concentration haloes are more strongly clustered than high concentration ones, while the trend at low masses is the inverse. The inversion occurs at a mass scale m_{inv} close to the characteristic mass for this cosmology $m_* = 2 \times 10^{13} h^{-1} M_\odot$ obtained from the peak of the halo mass distribution function and marked by the blue ar-

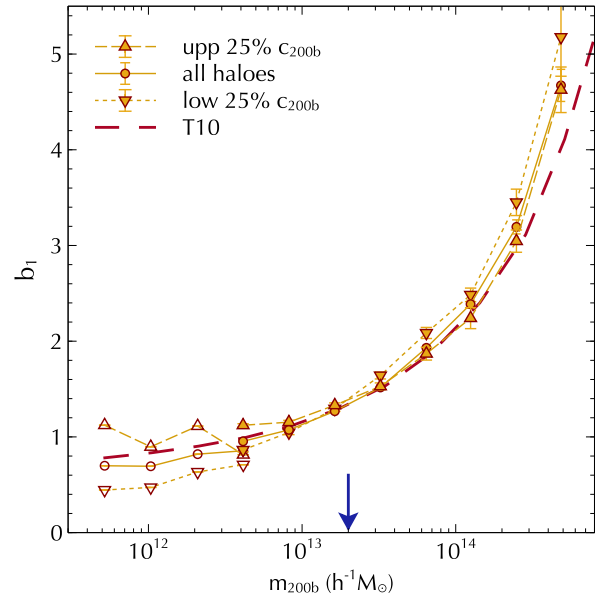


Figure 11. Traditional estimate of assembly bias, recovered by binning \hat{b}_1 in mass bins and splitting haloes by concentration quartiles as indicated. Filled symbols show the mean over 10 realisations of the default box and error bars indicate the standard error on the mean. The empty symbols joined by thin lines extending to low masses show the results of the single high resolution box. The arrow marks the characteristic mass m_* obtained from the peak of the halo mass distribution function. The small offset between the results of the default and high resolution boxes is almost certainly a volume effect, since the high resolution box cannot probe the small values of k required for an accurate estimate of \hat{b}_1 . We see the well known trend that, at high masses, low concentration haloes are more strongly clustered than high concentration ones, while the inverse is true at low masses.

row (see Paranjape & Padmanabhan 2017, for a discussion of the inversion scale obtained from different techniques).

We have also checked that we similarly reproduce previous results when haloes at fixed mass are split by their spin or shape (Bett et al. 2007; Faltenbacher & White 2010), using the halo spin parameter λ and minor-to-major axis ratio c/a of the halo shape ellipsoid, which are part of the default ROCKSTAR output catalogs. To avoid clutter, we do not display these results.

We next discuss how one can easily explore correlations between the large scale bias and variables linked to the tidal environment of haloes using the halo-by-halo bias variable \hat{b}_1 .

4.2 Assembly bias and tides

To begin with, we simply ask what happens to the assembly bias signal when haloes are split by their environment at $4R_{200b}$. The *left panel* of Figure 12 is formatted similarly to Figure 11, except that the larger (blue) symbols joined by thicker lines correspond to filamentary haloes and the smaller (yellow) symbols with thinner lines to node haloes. Clearly, filamentary haloes are more strongly clustered – more biased – than node halos of the same mass. Although we do not show it here, the dependence of \hat{b}_1 on the tidal environment is much stronger than when, e.g., halo

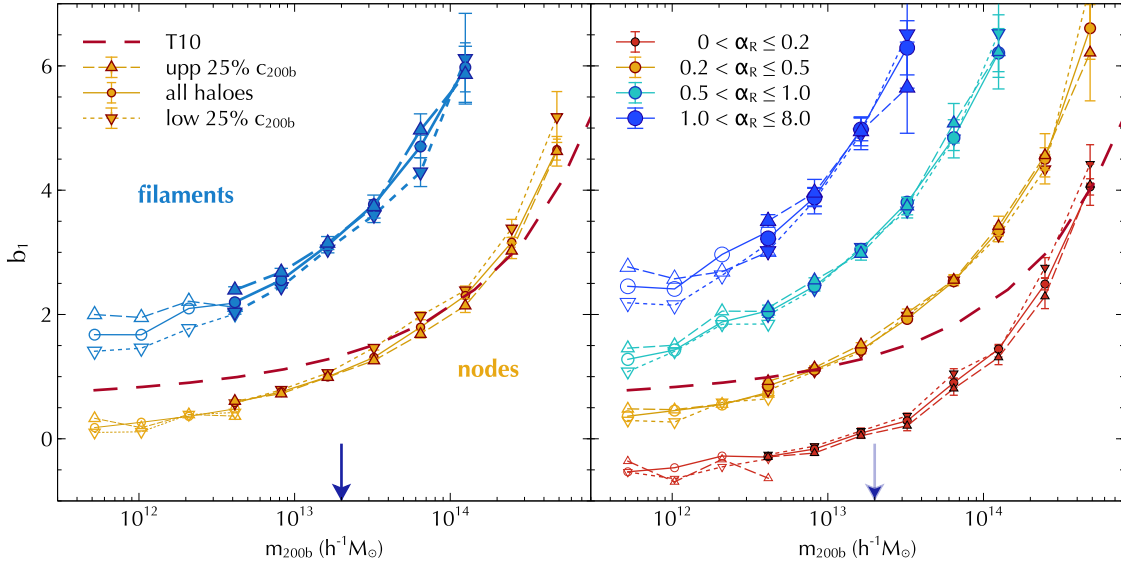


Figure 12. Assembly bias in different tidal environments. (*Left panel:*) Similar to Figure 11, but with results shown separately for haloes classified as being in nodes (smaller yellow symbols) and filaments (larger blue symbols) at the Gaussian equivalent of $4R_{200b}$. (*Right panel:*) Concentration-based assembly bias signature dissected as a function of α_R at $R = R_{G,eff}^{(4R_{200b})}$. Symbols of increasing size (with colours from red to blue) correspond to bins of increasing α_R as indicated. Formatting of point types (circles and triangles) is identical to that in the left panel. Filled symbols in each panel show the mean over 10 realisations of the default box and error bars indicate the standard error on the mean. The empty symbols joined by thin lines extending to low masses show the results of the single high resolution box. The arrow in each panel marks the characteristic mass m_* obtained from the peak of the halo mass distribution function, and smooth dashed curve shows the fitting function for linear bias appropriate for m_{200b} -haloes taken from Tinker et al. (2010). The left panel shows that the inversion of the assembly bias trend is largely restricted to haloes classified as being in filamentary local environments, as might be expected from the results of Hahn et al. (2009) and Borzyszkowski et al. (2017). The right panel shows that this transition happens smoothly as the tidal anisotropy α_R increases from small values (isotropic environments) to large values (anisotropic environments). See the main text and Figure 13 for further discussion.

shape is used (c.f. discussion at end of section 4.1). The increase of \hat{b}_1 as the environment becomes anisotropic is in good agreement with previous work (e.g. Hahn et al. 2009; Borzyszkowski et al. 2017). On the other hand, Faltenbacher & White (2010) report that \hat{b}_1 decreases as anisotropy increases. Although their environmental classification is based on the velocity- rather than tidal-shear, so quantitative differences might be expected, the qualitative difference in conclusions is surprising. We are in the process of checking if they simply mis-stated the correspondence between the velocity-shear based quantities they measured and the sphericity/isotropy of the environment.

In addition to the strong dependence on the anisotropy of the environment, filamentary haloes show a substantial assembly bias effect at nearly all masses probed, with high concentration haloes being more strongly clustered than low concentration ones. At the largest masses, the population is dominated by node haloes which, as expected, show the same trend as seen in Figure 11. The interesting point to note is that *low mass* node haloes continue to show the same trend as high mass node haloes, with *no inversion* around $m \sim m_*$. There is some hint of inversion at the smallest masses, where the signal strength considerably weakens.

To probe these environmental effects further, in the *right panel* of the Figure, instead of the node/filament split, we use bins of α_R with $R = R_{G,eff}^{(4R_{200b})}$, as in Figure 9. Similarly to the left panel, in each bin we show the mean \hat{b}_1 as a function of mass for all haloes in the bin (circles) and

for haloes in the upper and lower quartiles of concentration in that bin (upward and downward triangles, respectively). The all-halo results show a monotonic increase of \hat{b}_1 with α_R at all masses, consistent with the positive correlation seen in Figure 8. The results split by concentration clearly show that the low mass assembly bias trend is quite sensitive to the value of α_R , revealing a rather nuanced set of trends as a function of mass, α_R and concentration.

These trends are more easily described using an alternate representation of these results focusing on the *strength* of assembly bias. In Figure 13 we display the Spearman rank correlation between bias \hat{b}_1 and concentration c_{200b} as a function of halo mass, for haloes split into the same α_R bins as in Figure 12. To orient the discussion, note that, as expected, the all halo result (gray squares) shows a negative correlation at high masses which reverses sign and becomes positive at $m \lesssim m_*$ (c.f. Figure 11).

We see that there is essentially no *mass* dependence of the $\hat{b}_1 \leftrightarrow c_{200b}$ correlation for any α_R , except at the highest masses for $\alpha_R < 0.2$ (where the correlation becomes more negative) and at the lowest masses for $\alpha_R > 1.0$ (where the correlation becomes more positive). The *sign* of the signal, however, goes from negative to positive as α_R increases beyond ~ 0.2 at $m < m_*$, while at higher masses the signal becomes consistent with zero for $\alpha_R > 0.2$. The trend seen in node haloes in the left panel of Figure 12 is therefore revealed to be largely driven by haloes in only the most isotropic environments.

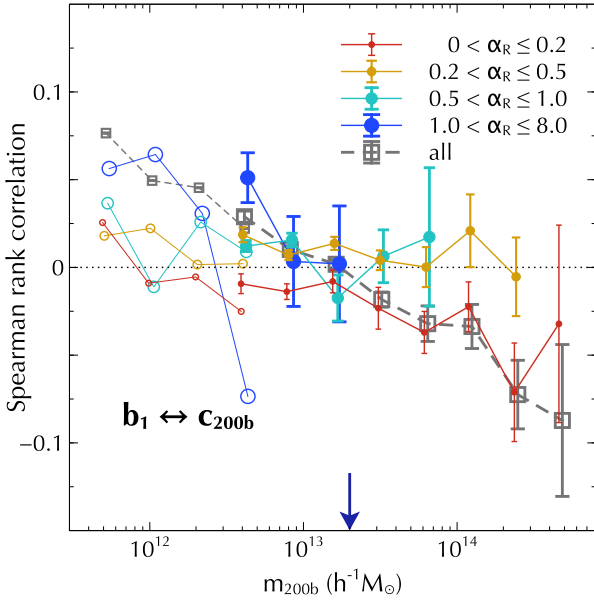


Figure 13. Spearman rank correlation coefficient between \hat{b}_1 and concentration c_{200b} , in bins of tidal anisotropy α_R at $R = R_{G,\text{eff}}^{(4R_{200b})}$. Note the difference in vertical scale as compared to Figures 3 and 8. Filled circles of increasing size correspond to increasing values of α_R as indicated, with the colour coding being identical to that in the right panel of Figure 12. Additionally, the empty gray squares show the result for all haloes. Results were averaged over 10 realisations of the default box and the error bars show the corresponding standard error on the mean. The empty symbols joined by thin lines extending to low masses show the results of the single high resolution box. For clarity, measurements in each bin of α_R were given small horizontal offsets. The arrow marks the characteristic mass m_* obtained from the peak of the halo mass distribution function. We see that the *sign* of the correlation at fixed α_R is nearly independent of halo mass and goes from negative to positive as α_R increases beyond ~ 0.2 . The overall trend for the all-halo sample at any fixed halo mass thus emerges as an average over halo populations with very different local tidal anisotropy. The criterion $\alpha_R < 0.2$ isolates a population of haloes closest to that described by the simplest excursion sets / peaks theory models (Dalal et al. 2008; Musso & Sheth 2012). See text for further discussion.

We also note in passing that, whereas plots such as those in Figure 12 can be made using traditional estimators of halo bias, the rank correlation measurements in Figure 13 (and Figure 8) are only possible with a halo-by-halo estimator of bias such as \hat{b}_1 . Figures 12 and 13 form the main results of this work, which we discuss in section 5 below.

5 DISCUSSION

The tidal environment of a halo is expected to play a significant role in determining the mass assembly history of the halo. Our definition of tidal anisotropy α_R (equation 10) evaluated at the Gaussian equivalent of $4R_{200b}$ (i.e., in the local halo environment) allows us to statistically quantify this connection, as we discuss next.

We have seen (Figure 8) that α_R is a better indicator of the *large scale* environment of haloes at fixed mass than is the density contrast δ_R smoothed on the same scale

$R \sim 4R_{200b}$. Specifically, haloes that live in anisotropic local environments tend to cluster more strongly than haloes of similar mass in more isotropic local environments (right panel of Figure 12). The variable α_R also has the nice property that it sharply distinguishes between node and filament environments as defined by counting the number of positive eigenvalues of the tidal tensor smoothed on the same scale, with the segregation occurring at $\alpha_R \simeq 0.5$ independent of halo mass (Figure 6).

Our main aim has been to understand the inversion of the halo assembly bias trend at low masses, where more concentrated haloes are clustered more strongly than less concentrated ones. This is the opposite of the trend predicted by simple peaks theory or excursion set models, which is in fact qualitatively realised at *high* masses. Previous studies suggest that this inversion is likely to be associated with the varying tidal environments of low mass haloes (Hahn et al. 2009; Borzyszkowski et al. 2017). We have seen in the left panel of Figure 12, in fact, that the low-mass inverted trend is largely restricted to haloes classified as being in filaments at $4R_{200b}$.

The tidal anisotropy α_R turns out to be a better indicator of the strength of the assembly bias signal than the node/filament split, functioning like a continuous knob rather than a binary switch that controls the sign and strength of the signal (right panel of Figure 12, and Figure 13). We see in Figure 13 that, for low mass haloes in the most isotropic environments ($\alpha_R \lesssim 0.2$), halo bias and concentration are weakly but significantly *anti*-correlated, just like for their high mass counterparts. The criterion $\alpha_R < 0.2$ has therefore isolated a population of haloes that is perhaps closest to that described by the simplest excursion sets / peaks theory models which ignore environmental anisotropy. It will be interesting to check whether the mass function of such objects is more universal than that of the full population of haloes (Tinker et al. 2008). The high mass end of this population contains the usual massive cluster-sized haloes, whereas the low mass end is dominated by objects in large scale sheets and voids (Figure 10; also c.f. the visualisation in Figure 7).

As the tidal anisotropy increases beyond $\alpha_R \simeq 0.2$, this small negative correlation turns positive (or, within the noise, consistent with zero at higher masses.) Overall, if we ignore any correlation between α_R and halo concentration, the traditional low-mass positive assembly bias signature in Figure 11, as well as the all-halo result in Figure 13, can be understood as arising because (a) the signal strength depends on α_R and (b) the fraction of low-mass haloes in environments with a negative signal ($\alpha_R \lesssim 0.2$) is subdominant (Figure 6).

This dependence of assembly bias sign and strength on tidal anisotropy strongly supports the idea that local tides dominate the mass assembly history of low mass haloes. Low mass haloes are comprised of two populations – those in highly isotropic environments which behave like ‘standard’ peaks-theory/excursion set haloes and those in anisotropic environments which show a *positive* correlation between concentration (or age) and large scale density.

There has been some analytical work on modelling the role of tidal effects on halo abundances and clustering (Shen et al. 2006; Sheth et al. 2013; Castorina et al. 2016). These studies fall within the context of the excursion set approach,

so they attempt to model how tidal effects in the *initial* field affect halo formation. Shen et al. (2006) focused on the roles played by the initial ellipticity and prolateness – in addition to the initial overdensity – of the protohalo patches which are destined to form virialized halos, whereas the more recent work has studied the role played by the initial tidal shear q associated with the protohalos. Our work suggests two important modifications to such studies: one is that α in the *evolved* field is the more relevant variable, and the other is that the relevant scale for these tidal effects may be *larger* than that of the protohalo. It will be interesting to see if, with these modifications, such excursion set based studies are able to exhibit the strong trends with α that are apparent in Figures 9 and 12. Moreover, although these previous studies have considered how bias depends on, e.g., q , they have not studied the correlation between the initial tidal shear of the protohalo patch and the concentration of the final halo – i.e., the additional assembly bias effect we highlighted in Figure 13. In a forthcoming paper (Musso et al., in preparation), we demonstrate how these populations can be analytically described in modified excursion set models.

We conclude this section with a brief discussion of potential applications of our analysis to real data. On the observational front, there has been considerable recent work on estimating the velocity and tidal fields in our local volume using, e.g., the Sloan Digital Sky Survey (SDSS) (Wang et al. 2012; Jasche & Wandelt 2013; Libeskind et al. 2015; Hoffman et al. 2017; Pomaredé et al. 2017) and performing constrained simulations of the local volume (Sorice et al. 2016; Wang et al. 2016). In the context of our analysis above, the galaxy group-based algorithm of Wang et al. (2012) is of particular interest, since the tidal field information derived from this algorithm could be used to calculate α_R for individual SDSS galaxy groups.

Given the connection between α_R and assembly bias that we have established in this work, we expect such an analysis to provide us an interesting new handle on *galaxy* assembly bias. Recent analyses of the SDSS main sample have shown that the observed level of assembly bias – as quantified by the correlation between large scale density and the fraction of (central) galaxies at fixed luminosity or stellar mass that are quiescent – is substantially below what is expected from the simplest models connecting galaxies to dark matter haloes (see, e.g. Tinker et al. 2016). While this could be due to underestimated scatter in the galaxy-dark matter connection in these models, it might also be the case that the SDSS sample does not sufficiently probe the anisotropic environments that dominate the theoretical signal. An analysis that accounts for local tidal anisotropy could conceivably distinguish between these possibilities. Another application of the tidal anisotropy could be to select environments sampling a broad range of large scale bias (c.f. Figure 12), which is relevant for multi-tracer analyses that aim to constrain primordial non-Gaussianity and/or detect large scale relativistic effects (see, e.g. McDonald & Seljak 2009; Hamaus et al. 2011; Fonseca et al. 2015). We intend to address these issues in the near future.

6 CONCLUSIONS

We have explored in detail the correlations between halo properties (mass and concentration) and halo environment, both local and large scale. In particular, we have quantified the nature of halo assembly in different environments by dissecting this signal according to the *anisotropy* α_R of the local tidal environment. Employing a novel halo-by-halo estimator of large scale bias, we have explored the correlations between halo properties and large scale bias, as a function of this local tidal anisotropy.

The picture that emerges from our multi-scale analysis involves *low mass* haloes varying between two regimes of local tidal anisotropy α_R . At one end are haloes in highly isotropic local environments ($\alpha_R \lesssim 0.2$), corresponding to underdensities at larger scales. These behave like scaled-down versions of their high mass counterparts, dominating their immediate environments and showing age-environment correlations qualitatively consistent with simple spherically averaged analytical expectations (namely, a negative correlation between concentration/age and large scale density). On the other side ($\alpha_R \gtrsim 0.2$) are haloes that live close to and are dominated by more massive objects, progressively more so with increasing α_R . These small haloes have highly *anisotropic*, filament-like local environments and show a *positive* correlation between concentration and large scale density.

The transition between isotropic and anisotropic environments, from the point of view of assembly bias strength, occurs at $\alpha_R \simeq 0.2$, which is below the threshold $\alpha_R \simeq 0.5$ demarcating the split between the more traditional definition of nodes and filaments (Figure 6). Figure 7 can be reviewed in this new light, with ‘anisotropic’ environments for the low mass haloes now corresponding to $\alpha_R \gtrsim 0.2$ (orange to blue circles). While we have focused on parent haloes in this work, it will be interesting probe the behaviour of halo substructure as a function of α_R ; in particular, whether α_R could be used as a discriminator of the population of so-called ‘backsplash’ haloes (Gill et al. 2005), which ought to have the highest values of α_R . We will explore this in future work, along with an extension of our analysis to higher redshifts.

ACKNOWLEDGEMENTS

AP gratefully acknowledges use of computing facilities at IUCAA, Pune. The research of AP is supported by the Associateship Scheme of ICTP, Trieste and the Ramanujan Fellowship awarded by the Department of Science and Technology, Government of India. OH acknowledges funding from the European Research Council (ERC) under the European Union’s Horizon 2020 research and innovation programme (grant agreement No. 679145, project ‘COSMO-SIMS’). AP thanks OCA, Nice for hospitality while part of this work was completed. We thank Marcello Musso for useful discussions.

REFERENCES

- Abbas U., Sheth R. K., 2007, *MNRAS*, **378**, 641
- Aragón-Calvo M. A., Jones B. J. T., van de Weygaert R., van der Hulst J. M., 2007, *A&A*, **474**, 315

Baldauf T., Seljak U., Desjacques V., McDonald P., 2012, *Phys. Rev. D*, **86**, 083540
 Bardeen J. M., Bond J. R., Kaiser N., Szalay A. S., 1986, *ApJ*, **304**, 15
 Behroozi P. S., Wechsler R. H., Wu H.-Y., 2013, *ApJ*, **762**, 109
 Behroozi P. S., Wechsler R. H., Lu Y., Hahn O., Busha M. T., Klypin A., Primack J. R., 2014, *ApJ*, **787**, 156
 Bett P., Eke V., Frenk C. S., Jenkins A., Helly J., Navarro J., 2007, *MNRAS*, **376**, 215
 Bond J. R., Myers S. T., 1996, *ApJS*, **103**, 1
 Borzyszkowski M., Porciani C., Romano-Díaz E., Garaldi E., 2017, *MNRAS*, **469**, 594
 Castorina E., Sheth R. K., 2013, *MNRAS*, **433**, 1529
 Castorina E., Paranjape A., Hahn O., Sheth R. K., 2016, preprint, ([arXiv:1611.03619](https://arxiv.org/abs/1611.03619))
 Castorina E., Paranjape A., Sheth R. K., 2017, *MNRAS*, **468**, 3813
 Catelan P., Theuns T., 1996, *MNRAS*, **282**, 436
 Chan K. C., Scoccimarro R., Sheth R. K., 2012, *Phys. Rev. D*, **85**, 083509
 Chan K. C., Sheth R. K., Scoccimarro R., 2017, *MNRAS*, **468**, 2232
 Dalal N., White M., Bond J. R., Shirokov A., 2008, *ApJ*, **687**, 12
 Desjacques V., 2008, *MNRAS*, **388**, 638
 Fakhouri O., Ma C.-P., 2010, *MNRAS*, **401**, 2245
 Faltenbacher A., White S. D. M., 2010, *ApJ*, **708**, 469
 Fonseca J., Camera S., Santos M. G., Maartens R., 2015, *ApJ*, **812**, L22
 Gao L., Springel V., White S. D. M., 2005, *MNRAS*, **363**, L66
 Gill S. P. D., Knebe A., Gibson B. K., 2005, *MNRAS*, **356**, 1327
 Gunn J. E., Gott III J. R., 1972, *ApJ*, **176**, 1
 Hahn O., Abel T., 2011, *MNRAS*, **415**, 2101
 Hahn O., Porciani C., Carollo C. M., Dekel A., 2007, *MNRAS*, **375**, 489
 Hahn O., Porciani C., Dekel A., Carollo C. M., 2009, *MNRAS*, **398**, 1742
 Hamaus N., Seljak U., Desjacques V., 2011, *Phys. Rev. D*, **84**, 083509
 Hearin A. P., Behroozi P. S., van den Bosch F. C., 2016, *MNRAS*, **461**, 2135
 Heavens A., Peacock J., 1988, *MNRAS*, **232**, 339
 Hoffman Y., Metuki O., Yepes G., Gottlöber S., Forero-Romero J. E., Libeskind N. I., Knebe A., 2012, *MNRAS*, **425**, 2049
 Hoffman Y., Pomarède D., Tully R. B., Courtois H. M., 2017, *Nature Astronomy*, **1**, 0036
 Jasche J., Wandelt B. D., 2013, *MNRAS*, **432**, 894
 Jing Y. P., Suto Y., Mo H. J., 2007, *ApJ*, **657**, 664
 Lazeyras T., Musso M., Schmidt F., 2017, *J. Cosmology Astropart. Phys.*, **3**, 059
 Leclercq F., Lavaux G., Jasche J., Wandelt B., 2016, *J. Cosmology Astropart. Phys.*, **8**, 027
 Lewis A., Challinor A., Lasenby A., 2000, *ApJ*, **538**, 473
 Libeskind N. I., Tempel E., Hoffman Y., Tully R. B., Courtois H., 2015, *MNRAS*, **453**, L108
 Lin Y.-T., Mandelbaum R., Huang Y.-H., Huang H.-J., Dalal N., Diemer B., Jian H.-Y., Kravtsov A., 2016, *ApJ*, **819**, 119
 McDonald P., Seljak U., 2009, *J. Cosmology Astropart. Phys.*, **10**, 007
 Miyatake H., More S., Takada M., Spergel D. N., Mandelbaum R., Rykoff E. S., Rozo E., 2016, *Physical Review Letters*, **116**, 041301
 Montero-Dorta A. D., et al., 2017, preprint, ([arXiv:1705.00013](https://arxiv.org/abs/1705.00013))
 Musso M., Sheth R. K., 2012, *MNRAS*, **423**, L102
 Paranjape A., Padmanabhan N., 2017, *MNRAS*, **468**, 2984
 Paranjape A., Sheth R. K., 2012, *MNRAS*, **419**, 132
 Pomarède D., Hoffman Y., Courtois H. M., Tully R. B., 2017, preprint, ([arXiv:1706.03413](https://arxiv.org/abs/1706.03413))

Saito S., Baldauf T., Vlah Z., Seljak U., Okumura T., McDonald P., 2014, *Phys. Rev. D*, **90**, 123522
 Schmidt F., Jeong D., Desjacques V., 2013, *Phys. Rev. D*, **88**, 023515
 Shen J., Abel T., Mo H. J., Sheth R. K., 2006, *ApJ*, **645**, 783
 Sheth R. K., Tormen G., 2002, *MNRAS*, **329**, 61
 Sheth R. K., Tormen G., 2004, *MNRAS*, **350**, 1385
 Sheth R. K., Chan K. C., Scoccimarro R., 2013, *Phys. Rev. D*, **87**, 083002
 Sorce J. G., et al., 2016, *MNRAS*, **455**, 2078
 Sousbie T., 2011, *MNRAS*, **414**, 350
 Springel V., 2005, *MNRAS*, **364**, 1105
 Tinker J., Kravtsov A. V., Klypin A., Abazajian K., Warren M., Yepes G., Gottlöber S., Holz D. E., 2008, *ApJ*, **688**, 709
 Tinker J. L., Robertson B. E., Kravtsov A. V., Klypin A., Warren M. S., Yepes G., Gottlöber S., 2010, *ApJ*, **724**, 878
 Tinker J., Wetzel A., Conroy C., Mao Y.-Y., 2016, preprint, ([arXiv:1609.03388](https://arxiv.org/abs/1609.03388))
 Wang H., Mo H. J., Yang X., van den Bosch F. C., 2012, *MNRAS*, **420**, 1809
 Wang H., et al., 2016, *ApJ*, **831**, 164
 Wechsler R. H., Zentner A. R., Bullock J. S., Kravtsov A. V., Allgood B., 2006, *ApJ*, **652**, 71
 Zentner A. R., Hearin A. P., van den Bosch F. C., 2014, *MNRAS*, **443**, 3044
 Zu Y., Mandelbaum R., Simet M., Rozo E., Rykoff E. S., 2016, preprint, ([arXiv:1611.00366](https://arxiv.org/abs/1611.00366))

APPENDIX A: USEFUL SCALING RELATIONS

In this Appendix we note down some useful scalings between various quantities that define our N -body simulations and their analysis.

A1 Halo mass and grid

Consider a simulation in a cubic box with comoving length L_{box} , matter density parameter Ω_m and number of particles N_p . Since the critical density at present epoch is $\rho_{\text{crit},0} = 3H_0^2/(8\pi G) = 2.7754 \times 10^{11} h^{-1} M_\odot / (h^{-1} \text{Mpc})^3$, a halo resolved with $N_p^{(\text{halo})}$ particles will have a mass M_{halo} given by

$$M_{\text{halo}} = 3.8524 \times 10^{11} h^{-1} M_\odot \left(\frac{N_p^{(\text{halo})}}{200} \right) \left(\frac{1024^3}{N_p} \right) \times \left(\frac{\Omega_m}{0.276} \right) \left(\frac{L_{\text{box}}}{300 h^{-1} \text{Mpc}} \right)^3. \quad (\text{A1})$$

If this mass corresponds to m_{200b} , the mass enclosed in a radius R_{200b} where the enclosed density is 200 times the background density, then we can write

$$\begin{aligned} R_{200b} &= 181.7 h^{-1} \text{kpc} \left(\frac{L_{\text{box}}}{300 h^{-1} \text{Mpc}} \right) \\ &\times \left(\frac{N_p^{(\text{halo})}}{200} \right)^{1/3} \left(\frac{1024}{N_p^{1/3}} \right) \\ &= 678.0 h^{-1} \text{kpc} \left(\frac{M_{\text{halo}}}{2 \times 10^{13} h^{-1} M_\odot} \right)^{1/3} \left(\frac{0.276}{\Omega_m} \right)^{1/3} \end{aligned} \quad (\text{A2})$$

where we have normalised the halo mass by the $z = 0$ characteristic mass for our fiducial cosmology. If we impose a cubic grid on the box with N_g cells for post-processing, then the

comoving length $\Delta x = L_{\text{box}}/N_g^{1/3}$ of each grid cell can be written as

$$\Delta x = 585.9 h^{-1} \text{kpc} \left(\frac{L_{\text{box}}}{300 h^{-1} \text{Mpc}} \right) \left(\frac{512}{N_g^{1/3}} \right). \quad (\text{A4})$$

The number of these grid cells enclosed in a sphere of radius $2R_{200b}$ centered on a halo is given by

$$\begin{aligned} N_{\text{encl}}(< 2R_{200b}) &\equiv (4\pi/3)(2R_{200b})^3/(\Delta x)^3 \\ &= 1 \times \left(\frac{N_p^{(\text{halo})}}{200} \right) \left(\frac{1024^3}{N_p} \right) \left(\frac{N_g}{512^3} \right). \end{aligned} \quad (\text{A5})$$

We can then write

$$\begin{aligned} M_{\text{halo}} &= 3.0819 \times 10^{12} h^{-1} M_{\odot} \left(\frac{N_{\text{encl}}(< 2R_{200b})}{8} \right) \\ &\times \left(\frac{512^3}{N_g} \right) \left(\frac{\Omega_m}{0.276} \right) \left(\frac{L_{\text{box}}}{300 h^{-1} \text{Mpc}} \right)^3. \end{aligned} \quad (\text{A6})$$

For the configuration we use in the main text ($N_g = 512^3$, $\Omega_m = 0.276$, $L_{\text{box}} = 300 h^{-1} \text{Mpc}$), demanding that twice R_{200b} for a halo be resolved with at least 8 grid cells then gives a minimum halo mass of $m_{\text{min}} \simeq 3.1 \times 10^{12} h^{-1} M_{\odot}$ or $N_p^{(\text{halo})} \geq 1600$. Note that this grid is used only in post-processing the simulation, and is much coarser than the 2048^3 grid used for PM calculations in the simulation.

A2 Gaussian smoothing

In practice, we will use Gaussian smoothing kernels to define, e.g., the tidal tensor in the simulation. Since the widths of Gaussian and Tophat smoothing windows are different for the same smoothing radius, one must be careful to account for this difference. This is most easily done by Taylor expanding the Fourier transform of each window and matching the first non-trivial term in each (proportional to $k^2 R^2$). This gives the relation

$$R_G \approx R_{\text{TH}}/\sqrt{5} \quad (\text{A7})$$

Denoting the Gaussian equivalent of $2R_{200b}$ by $R_{G,\text{eff}}^{(2R_{200b})} = 2R_{200b}/\sqrt{5}$, we find the relations

$$\begin{aligned} R_{G,\text{eff}}^{(2R_{200b})} &= 162.5 h^{-1} \text{kpc} \left(\frac{L_{\text{box}}}{300 h^{-1} \text{Mpc}} \right) \\ &\times \left(\frac{N_p^{(\text{halo})}}{200} \right)^{1/3} \left(\frac{1024}{N_p^{1/3}} \right) \end{aligned} \quad (\text{A8})$$

$$= 606 h^{-1} \text{kpc} \left(\frac{M_{\text{halo}}}{2 \times 10^{13} h^{-1} M_{\odot}} \right)^{1/3} \left(\frac{0.276}{\Omega_m} \right)^{1/3} \quad (\text{A9})$$

$$\begin{aligned} &= 325 h^{-1} \text{kpc} \left(\frac{N_{\text{encl}}(< 2R_{200b})}{8} \right)^{1/3} \\ &\times \left(\frac{512}{N_g^{1/3}} \right) \left(\frac{L_{\text{box}}}{300 h^{-1} \text{Mpc}} \right). \end{aligned} \quad (\text{A10})$$

Note that, for any constant K , we have

$$R_{G,\text{eff}}^{(K R_{200b})} = (K/2) R_{G,\text{eff}}^{(2R_{200b})}. \quad (\text{A11})$$

In the main text, we require the tidal environment at the Gaussian equivalent of $2R_{200b}$, $4R_{200b}$, etc. In practice, these

are calculated by first measuring the tidal tensor using a series of fixed Gaussian radii and then interpolating the results to the scale corresponding to each halo using, e.g., equation (A9). Equation (A10) then says that the minimum Gaussian radius in this series of windows should be $325 h^{-1} \text{kpc}$ when considering haloes resolved by at least 8 grid cells inside $2R_{200b}$. We have checked that the results have safely converged when using 15 equi-log spaced values of Gaussian radius for the interpolation.

APPENDIX B: TIDAL TENSOR AND TIDAL ENVIRONMENT

The tidal tensor at smoothing scale R (we assume Gaussian smoothing throughout), is defined as

$$T_{ij}(\mathbf{x}) = \partial_i \partial_j \psi_R(\mathbf{x}) \quad (\text{B1})$$

where the normalised, smoothed gravitational potential $\psi_R(\mathbf{x})$ obeys the Poisson equation

$$\nabla^2 \psi_R(\mathbf{x}) = \delta_R(\mathbf{x}). \quad (\text{B2})$$

As described in the main text, the smoothed density contrast $\delta_R(\mathbf{x})$ is obtained in Fourier space as $\delta_R(\mathbf{k}) = \delta(\mathbf{k}) e^{-k^2 R^2/2}$, where $\delta(\mathbf{k})$ is the Fourier transform of the CIC interpolated real space quantity $\delta(\mathbf{x})$. In terms of the Fourier variables above, the tidal tensor is

$$T_{ij}(\mathbf{x}) = \text{FT} \left\{ (k_i k_j / k^2) \delta(\mathbf{k}) e^{-k^2 R^2/2} \right\}. \quad (\text{B3})$$

Denoting the eigenvalues of T_{ij} by $\lambda_1 \leq \lambda_2 \leq \lambda_3$, the tidal classification of the halo environment at scale R can be summarised as (Hahn et al. 2007):

$$\begin{aligned} \lambda_1 &> 0 : \text{node} \\ \lambda_1 < 0 \ \&\ \lambda_2 > 0 : \text{filament} \\ \lambda_2 < 0 \ \&\ \lambda_3 > 0 : \text{sheet} \\ \lambda_3 &< 0 : \text{void} \end{aligned} \quad (\text{B4})$$

APPENDIX C: ANALYTICAL ARGUMENTS

In this Appendix, we present some simple analytical arguments that clarify some of the trends discussed in the main text.

C1 Correlation between \hat{b}_1 and large scale density

Our definition of halo-by-halo bias \hat{b}_1 in equation (8) is closely linked to the density field filtered on large scales using a sharp filter in Fourier space. This is easily seen by noting that, had we replaced N_k with $P_{\text{mm}}(k)$ in that equation – i.e., weighted by the power spectrum rather than number of k -modes – we would have obtained the ratio of the sharp- k filtered conditional density contrast and the variance of its unconditional counterpart. This also shows that \hat{b}_1 is conceptually identical to the quantity written down by Paranjape & Sheth (2012) in their equation (22) in the context of deriving halo bias from excursion set models, except that Paranjape & Sheth (2012) were working with the Lagrangian field while \hat{b}_1 is defined for the Eulerian field (see

also [Castorina et al. 2017](#); [Chan et al. 2017](#), for generalisations to include multiple constraints on the haloes).

We can take this comparison further and understand the size of the scatter in Figure 1 and the correlation trends in Figure 3 using some simplified models. To explain the size of the scatter, consider the Gaussian approximation in which the conditional distribution $p(\delta_R|\text{halo})$ is a Gaussian with mean $\langle \delta_R|\text{halo} \rangle = (S_\times/S_{\text{halo}})\delta_{\text{halo}} = S_\times b_1$ and variance $\text{Var}(\delta_R|\text{halo}) = S_R - S_\times^2/S_{\text{halo}}$. Here $S_R = \langle \delta_R^2 \rangle$ is the unconditional variance on scale $R \sim 1/k_{\text{max}}$ for sharp- k filtering, $S_{\text{halo}} = \langle \delta_{\text{halo}}^2 \rangle$ the unconditional variance on scale $R_{\text{halo}} \ll R$ and $S_\times = \langle \delta_R \delta_{\text{halo}} \rangle$ is the cross-correlation term. For sharp- k filtering, we have $S_\times = S_R$, so that $\langle \delta_R|\delta_{\text{halo}} \rangle = S_R b_1$ and $\text{Var}(\delta_R|\delta_{\text{halo}}) = S_R(1 - S_R/S_{\text{halo}}) \simeq S_R$. Since we display b_1 in this analogy rather than $S_R b_1$, the variance around the mean should be $S_R(1 - S_R/S_{\text{halo}})/S_R^2 = 1/S_R - 1/S_{\text{halo}} \simeq 1/S_R$, with little dependence on halo mass. Setting $k_{\text{max}} = 0.09 h \text{Mpc}^{-1}$ and using the linear theory power spectrum for our cosmology gives us $S_R \sim 0.13$, or a standard deviation of ~ 2.8 in b_1 . This compares quite well with the measured standard deviation of $\simeq 3$ in \hat{b}_1 .

To explain the trends in Figure 3, we can simply note that, for large enough R , \hat{b}_1 and δ_R are essentially measuring the same variable and must therefore be positively correlated with a strength that increases with R . Alternatively, consider a second simplified model which explicitly models the dependence of \hat{b}_1 on the Gaussian filtered δ_R . In this model, the bias is given by $b_1 = \delta_{\text{Lag}}/S(R_{\text{Lag}})$ where R_{Lag} is the scale which contains mass $\bar{\rho}(2\pi)^{3/2}R^3(1 + \delta_R)$, $S(R_{\text{Lag}})$ is the sharp- k variance on this scale and $\delta_{\text{Lag}} = \delta_c \left(1 - (1 + \delta_R)^{-1/\delta_c}\right)$, which follows from an approximation to spherical collapse. At fixed R , as δ_R increases, δ_{Lag} and R_{Lag} increase, so that $S(R_{\text{Lag}})$ decreases and hence b_1 increases, which is qualitatively consistent with the left panel of Figure 3. To explain the right panel, we must compute the correlation coefficient between b_1 and δ_R in this model. Assuming that both these variables are Gaussian and Taylor expanding all expressions to 4th order in δ_R , we find the correlation coefficient $r_{b_1 \delta_R} \simeq 1 - 0.1S_R + 0.7S_R^2$ independent of halo mass; as expected, the coefficient approaches unity as R increases.

C2 Physical significance of $4R_{200b}$

Consider a spherically symmetric overdense region obeying spherical collapse ([Gunn & Gott 1972](#)) and forming a virialised structure of mass M , radius R and overdensity $\Delta = \rho(< R)/\bar{\rho} \approx 200$ at $z = 0$, where $\rho(< R) = M/(4\pi R^3/3)$ is the density enclosed inside radius R and $\bar{\rho}$ is the mean density of the Universe. Let us now ask for the radius R_{ta} of the spherical shell around this halo which is currently (i.e., at $z = 0$) decoupling from the Hubble flow and turning around. According to the spherical model, R_{ta} encloses a density $\rho(< R_{\text{ta}}) \simeq 5.5\bar{\rho}$, so that we can write

$$\begin{aligned} 5.5 &\simeq \rho(< R_{\text{ta}})/\bar{\rho} = \frac{1}{\bar{\rho}} \left(\frac{M + M_{\text{out}}}{4\pi R_{\text{ta}}^3/3} \right) \\ &= \Delta \left(\frac{R}{R_{\text{ta}}} \right)^3 + \frac{M_{\text{out}}/\bar{\rho}}{4\pi R_{\text{ta}}^3/3}, \end{aligned} \quad (\text{C1})$$

where we split the mass enclosed in R_{ta} into the mass M in the halo and the mass M_{out} outside it. If the matter sur-

rounding the halo were unclustered, then we would have $M_{\text{out}}/\bar{\rho} = 4\pi(R_{\text{ta}}^3 - R^3)/3$, leading to

$$R_{\text{ta}}/R \simeq (\Delta/(5.5 - 1))^{1/3} \simeq 3.5. \quad (\text{C2})$$

Clustering will increase the value of M_{out} and therefore push R_{ta} to somewhat larger values. Numerical evaluations of the spherical model using reasonable initial density profiles lead to values of R_{ta}/R between ~ 4 -6. This could plausibly be related to our finding in the main text that the correlation strength between large scale bias and local tidal anisotropy peaks at around $4R_{200b}$, nearly independently of halo mass.